Omnidirectional Channel Sounder With Phased-Array Antennas for 5G Mobile Communications

Derek Caudill, Peter B. Papazian, *Senior Member, IEEE*, Camillo Gentile, *Member, IEEE*, Jack Chuang, and Nada Golmie

***Abstract*— We describe a 60-GHz channel sounder with phased-array antennas and 1-GHz bandwidth. It estimates the angle of departure (AoD)/angle of arrival (AoA) of channel multipath components (MPCs) by sweeping the antenna space of the transmitter/receiver through 5.6° electronically steerable beams. The associated 26.1-dBi gain and resultant 36-dBm EIRP of the beams enable sounding up to hundreds of meters. Both ends integrate multiple arrays to extend the ±45° field of view (FoV) of the individual arrays to an omnidirectional view; the additional advantage of integrating multiple arrays is to quicken the channel sweep period to just 262 μs, corresponding to a maximum closing velocity of 33 km/h for vehicle-to-vehicle (V2V) scenarios. The receiver is mounted on a mobile robot whose navigational system enables rapid, autonomous, and untethered data collection. Over-the-air (OTA) methods to characterize the array beams patterns, calibrate the system impulse response, and compensate for clock drift are proposed such that properties of the MPCs can be extracted with high fidelity through super-resolution techniques. To substantiate the latter, we compare estimated properties against ground-truth values from extensive field measurements. The mean absolute error in angle was reported as 2.87°.**

***Index Terms*— Double directional, over-the-air (OTA) calibration, 60 GHz, super-resolution.**

I. Introduction

THE exponential increase in wireless data transmission from smartphones has led to the saturation of the sub-6-GHz bands—where 4G cellular networks operate today—driving the investigation of millimeter-wave (mmWave) frequencies for 5G communications. As a result, in July 2016, the Federal Communications Commission (FCC) released nearly 11 GHz of spectrum in the 28–73-GHz band for terrestrial communications, and an additional 17.7 GHz is currently under review [1]. Although free-space loss, penetration loss, and oxygen-absorption loss around 60 GHz are notably greater, the bandwidth available per channel is tens of gigahertz [2]. To enable the link distances up to hundreds of meters, the greater path loss will be compensated by highly directional antennas with 20–40-dBi gain. Since beamwidth is inversely proportional to gain, the antennas will feature 3°–15° pencilbeams. Hence, to render omnidirectional field of view (FoV), the transmit and receive beams will be electronically steered along the respective angle of departure (AoD) and angle of arrival (AoA)—jointly referred to as double-directional angle—of any viable propagation paths between the two. Therefore, it is essential for 5G channel models to capture the angular properties of the channel.

In addition to high path loss, another property of mmWave channels is weak diffraction [3], rendering direct transmission and specular reflection the chief propagation mechanisms. Furthermore, diffuse reflections from surface roughness must be accounted for since the roughness is comparable in size to the wavelength. Diffuse reflections cluster densely around specular reflections in the delay-angle space of the paths and so, when the transceivers steer their beams toward the specular paths, they will inevitably detect diffuse paths as well, giving rise to fading [4]. In [5], it is shown that the angular spread of clusters is between 3° and 4°; hence, to discriminate diffuse paths, mmWave channel sounders must have angular resolution on the order of degrees.

Finally, since 5G applications will include outdoor deployment, such as in urban-canyon environments, channel sounders must be able to handle vehicular speed even for fixed point-to-point deployment, not to mention more avant-garde vehicle-to-vehicle (V2V) scenarios. As such, sounders must be fast enough to sample the channel within the coherence time—the time during which the channel is considered stationary—which is on the order of milliseconds [6].

In summary, to be effective, 5G channel sounders must satisfy the following key criteria.

1) *Ultrawide Bandwidth:* 1–10 GHz to characterize the instantaneous channel allocation envisioned for 5G applications.
2) *High Antenna Gain:* 20–40-dBi gain to enable sounding to hundreds of meters.
3) *Omni-Double Directionality:* Antenna arrays integrated at both transmit and receive ends that provide omnidirectional view in AoD and AoA.
4) *High Angular Resolution:* On the order of 1°–3° to discriminate diffuse channel components.
5) *Fast Channel Sweep Period:* On the order of milliseconds for mobile environments.

The most common approach to sound mmWave channels to date has been to equip the transmitter and receiver with

Manuscript received December 21, 2018; revised March 15, 2019; accepted March 19, 2019. Date of publication April 24, 2019; date of current version July 1, 2019. *(Corresponding author: Camillo Gentile.)*

D. Caudill and P. B. Papazian are with the RF Technology Division, National Institute of Standards and Technology, Boulder, CO 80305 USA.

C. Gentile, J. Chuang, and N. Golmie are with the Wireless Networks Division, National Institute of Standards and Technology, Gaithersburg, MD 20899 USA (e-mail: camillo.gentile@nist.gov).

Color versions of one or more of the figures in this paper are available online at http://ieeexplore.ieee.org.

Digital Object Identifier 10.1109/TMTT.2019.2910109

a single horn antenna at each end [7]–[15]. The AoD and AoA are swept through the mechanical rotation of the horns to obtain a different channel response for each pair of look angles. The angular resolution, however, is limited to the beamwidth of the antennas, which is typically 10°–20°. More advanced approaches [16] mechanically translate the horns on positioners, forming virtual planar arrays. The half-wavelength spacing between positions on a grid-like structure, equivalent to the Nyquist sampling rate, enables the coherent phase combination to deliver super-resolution—resolution beyond the inherent beamwidth of the antennas—on the order of degrees. The problem with the aforementioned systems is that mechanical rotation/translation is notoriously slow and a single channel acquisition can take hours, limiting measurements campaigns to typically tens of acquisitions in static environments.

On the contrary, electronically switched arrays can be very fast. For example, the 16×8 system in [17] employs multiple directional horns at each end that when synthesized span the omnidirectional azimuthal space and 45° in elevation. All 128 channels can be swept within 262 μs to support scenarios up to a closing velocity of 33 km/h. However, since the elements are too bulky for the Nyquist spacing, coherent phase combination between them is not possible; they nevertheless render angle estimation on the order of degrees. The 16×1 [19], 2×2 [20], and 8×8 [21] systems are similar in design.

Phased-array antennas [22] generate electronically steerable beams by phasing the individual elements of the array, and thus offer enhanced flexibility in terms of beamwidth and beam orientation compared to fixed horns. With half-wavelength spacing between the patch antennas, coherent phase combination to deliver extremely high angular fidelity—like virtual arrays—is possible. The number of elements per array typically ranges between 16 and 64, so their collective gain is above 25 dBi. Finally, the arrays feature bandwidths up to 2 GHz and have beam switching time on the order of microseconds. This qualifies them to meet all necessary criteria for 5G channel sounding.

The main contributions of this paper are as follows.

1) A 60-GHz phased-array-antenna channel sounder with 1-GHz bandwidth.
2) System with a mobile robot at the receiver whose indoor and outdoor navigational systems enables rapid, autonomous, and untethered data collection.
3) Multiple arrays at both the transmitter and receiver synchronized through rubidium clocks to make possible an omni-double-directional channel sweep in milliseconds.
4) Application of high precision over-the-air (OTA) methods to characterize the array beam patterns, calibrate the system impulse response, and compensate for the phase drift of the clocks to support super-resolution techniques for multipath-component (MPC) extraction, yielding 2.87° mean absolute error in angle estimation.

We are aware of only three other channel sounders integrating phased-array antennas: Weiler et al. [23] make the first claim; however, the 60-GHz system features a single array (at the receiver) whose primitive antenna pattern offers only 3.4-dB sidelobe suppression. Bas *et al.* [24] operate at a center frequency of 28 GHz and with a bandwidth of 400 MHz, ±45° FoV due to single arrays at both ends, and no OTA methods for precision system calibration. Similarly, Slezak *et al.* [25] utilize a single array at both ends with ±45° FoV in a static setup for human blockage experiments at 60 GHz.

This paper is organized as follows. In Section II, we describe our active phased-array-antenna boards and the transmit and receive sections driving the boards, followed by Section III proposing OTA calibration methods. In Section IV, we describe the super-resolution technique used to extract the channel MPCs from field measurements and present companion results. Finally, we conclude with avenues for further research.

II. System Architecture

In this section, we describe the main system components of our channel sounder, namely the phased-array antennas, the transmit and receive sections, and the mobile robot used for autonomous data collection.

A. Phased-Array Antennas

The active phased-array-antenna boards integrated in our channel sounder are described in specific detail in [22]; our intention here is to highlight their main properties only. Their exact center frequency is 62.5 GHz ($\lambda = 4.8$ mm), and their null-to-null passband is 2 GHz. Fig. 1(a) displays one of the boards: it is composed from 8×32 microstrip patch antennas spaced at 0.54λ and polarized in the elevation plane only. The only difference from [22] is that the board has two RF ports—not just one—effectively splitting it into two 8×16 arrays for enhanced implementation flexibility. Each column of eight elements has a single vector-modulated based phase shifter (5-bit quantizer) and a single variable-gain amplifier (4-bit quantizer); this means that the arrays can be steered in the azimuth plane only. The nominal half-power scan range is ±45°. The purpose of multiple elements per column is to increase gain; in fact, the elements are visibly tapered at the edges for optimal performance. At boresight, nominally the gain is 26.1 dBi, the azimuth beamwidth is 5.6°, and the elevation beamwidth is 11.6°.

Each RF port has a companion mixer for up-/downconversion and local-oscillator (LO) doublers. LO distribution, mixers, and doublers are in the lower section of the assembly. The large external fan (black box) per board is critical for heat dissipation. Absorber has been applied to the metal plates below the antennas to minimize reflection from the system into the measured channel.

B. Transmit Section

Since each array can only scan ±45°, two boards are arranged at a right angle at the transmitter (Tx), as shown in Fig. 1(b), to render a combined 180° FoV. The Tx is fixed on a tripod and with its “blind side” oriented away from the receiver (Rx), so the limited FoV is acceptable. Both arrays per board are exploited to halve the channel sweep period by concurrently scanning the positive and negative steer angles within the ±45° range. Details on the channel sweep are

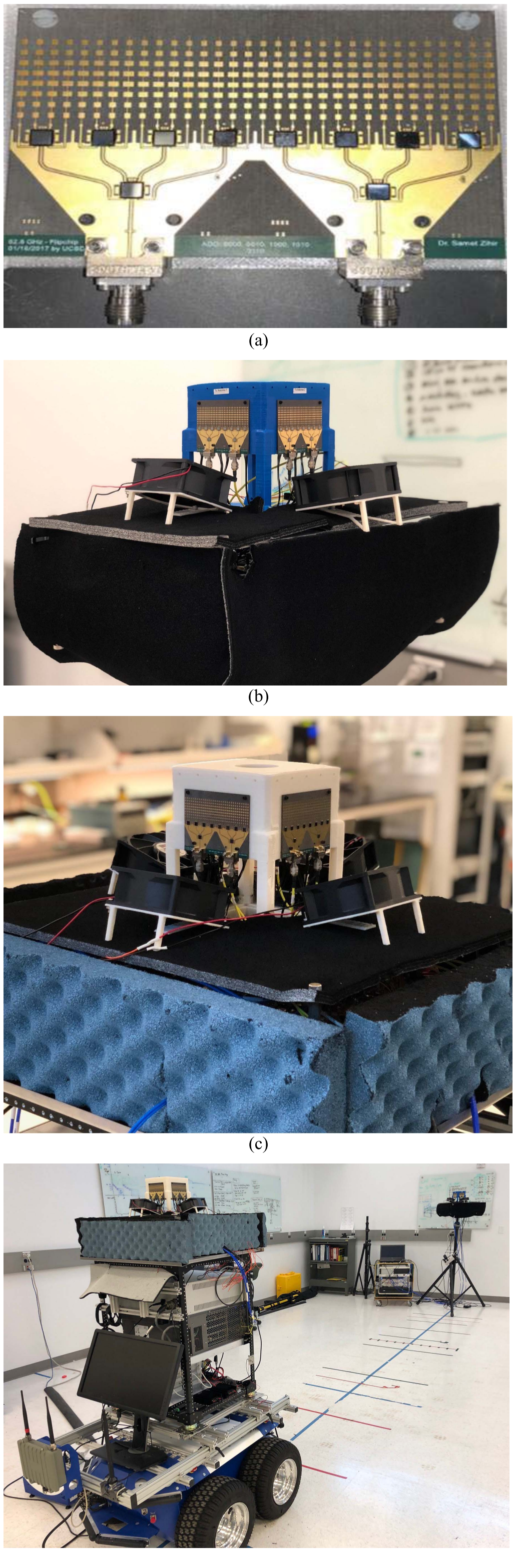

Fig. 1. (a) 62.5-GHz active phased-array-antenna board. The board features two 8×16 arrays with separate RF feeds. (b) Transmit section. Two antenna-array boards, each with $\pm 45°$ scan range, are mounted at a right angle to provide 180° FoV. (c) Receive section. Four antenna boards, each with $\pm 45°$ scan range, are mounted at right angles to provide 360° FoV. (d) Transmit section mounted on a tripod and receive section mounted on the mobile robot in our laboratory.

provided later. A block diagram of the Tx section is shown in Fig. 2(a).

The arbitrary waveform generator (AWG) at the Tx has four channels to accommodate the four arrays. It continuously generates a repeating BPSK-modulated pseudorandom-noise (PN) code with 1-ns chip length—corresponding to 1-GHz half-power bandwidth—and 2047 chips. The code is synthesized at an intermediate frequency (IF) of 2.5 GHz, followed by a 2-GHz bandpass filter; the filter truncates the signal beyond its first lobe to avoid overlap with adjacent bands. The signal is then upconverted to 62.5 GHz and sent over the antennas with an EIRP of 36 dBm.

C. Receive Section

In contrast to the Tx, omnidirectional view is critical at the Rx because it is mounted on a mobile robot and so must be able to "see" from all directions. To that end, four boards—not just two—were arranged at right angles. Fig. 1(c) shows a photograph of the receive section, and Fig. 2(b) shows its block diagram. As with the Tx, both arrays per board are exploited to scan the positive and negative steer angles within the $\pm 45°$ scan range concurrently. To accommodate this, the Rx digitizer has eight channels. The RF signal per channel is downconverted back to IF and digitized directly at a rate of 40 GHz, as opposed to on-the-fly correlation that some channel sounders implement [10]. While the latter enjoys a lower noise floor due to the smaller 0.4-GHz bandwidth, the advantage of the former is that correlation is performed in postprocessing so that the channel can be sampled quicker. The digitized signal is then match filtered with the known PN code—with associated processing gain of 33 dB—to yield the channel impulse response. No averaging for additional processing gain is applied.

D. Channel Sweep

A channel acquisition consists of sweeping through all Tx and Rx steer angles pairwise and recording the impulse response for each. The increment in the steer angle is 5.6°, equivalent to the nominal beamwidth of the arrays. Hence, to scan the $\pm 45°$ range per board, 16 angles—eight angles per array covering $+45°$ and $-45°$ each—are swept. Each array has a dedicated serial peripheral interface (SPI) controller to steer its beam. The SPI program time—roughly 50 μs—is the bottleneck of the system; so to reduce the channel sweep period, the four Tx arrays and eight Rx arrays are programmed simultaneously—each program assigning a set of four Tx angles and a set of eight Rx angles. The sets are depicted in Fig. 3(a). Since there are eight unique Tx sets and eight unique Rx sets, there is a total of 64 unique Tx–Rx sets.

Synchronization between the Tx and Rx sections is necessary to maintain simultaneous programming of the arrays' SPIs and triggering of the Rx digitizer in sync with transmission of the PN code. Synchronization is realized through a timing circuit based on the pulse-position modulation (PPM) with rubidium clocks at each end. Because the code is transmitted continuously at the Tx, the fundamental time slot of the circuit is set to the code length, 2047 ns. The channel sweep schedule is depicted in Fig. 3(b): 32 slots are required to scan a Tx set or Rx set—one for trigger setup, 26 to program the steering weights, and four for transmission (one is a buffer). Time-division multiplexing is implemented to transmit the code

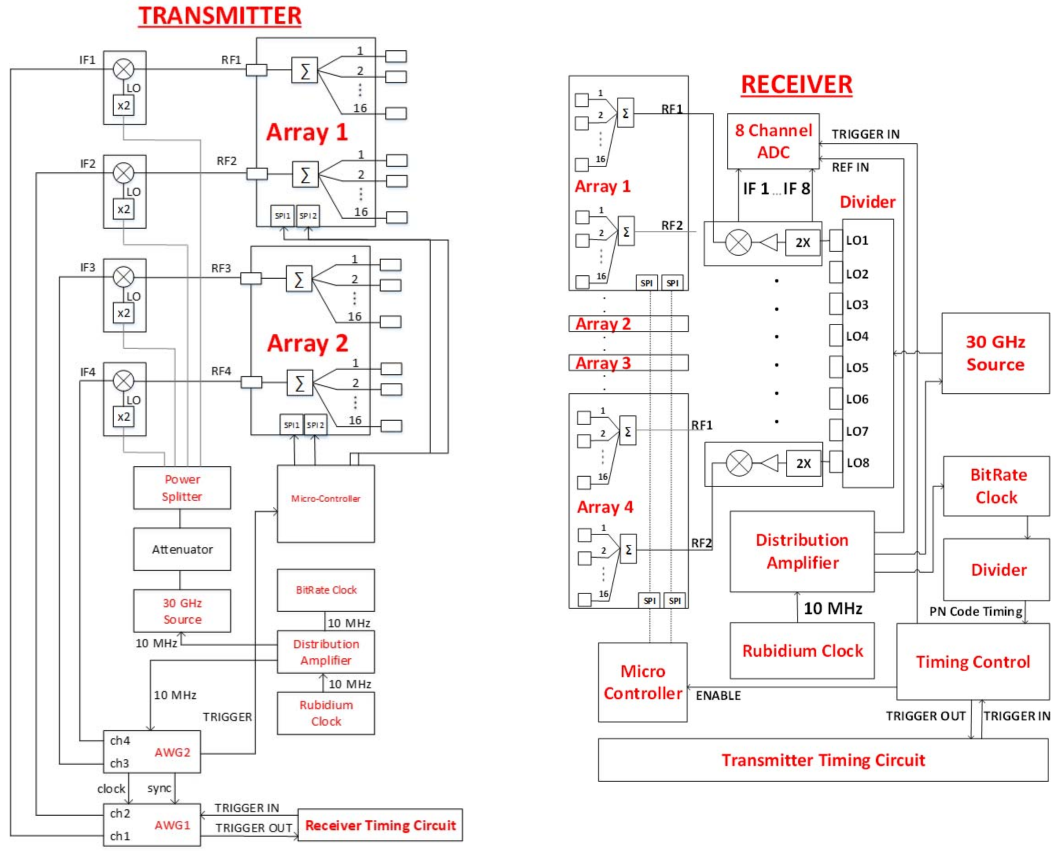

(a) (b)

Fig. 2. (a) Transmitter block diagram. The transmitter has two boards, each with ±45° FoV, arranged at a right angle to scan 180°. Each board has two arrays with separate RF ports, allowing concurrent operation. (b) Receiver block diagram. The receiver has four boards arranged at right angles to scan 360°; hence, it has a total of eight arrays.

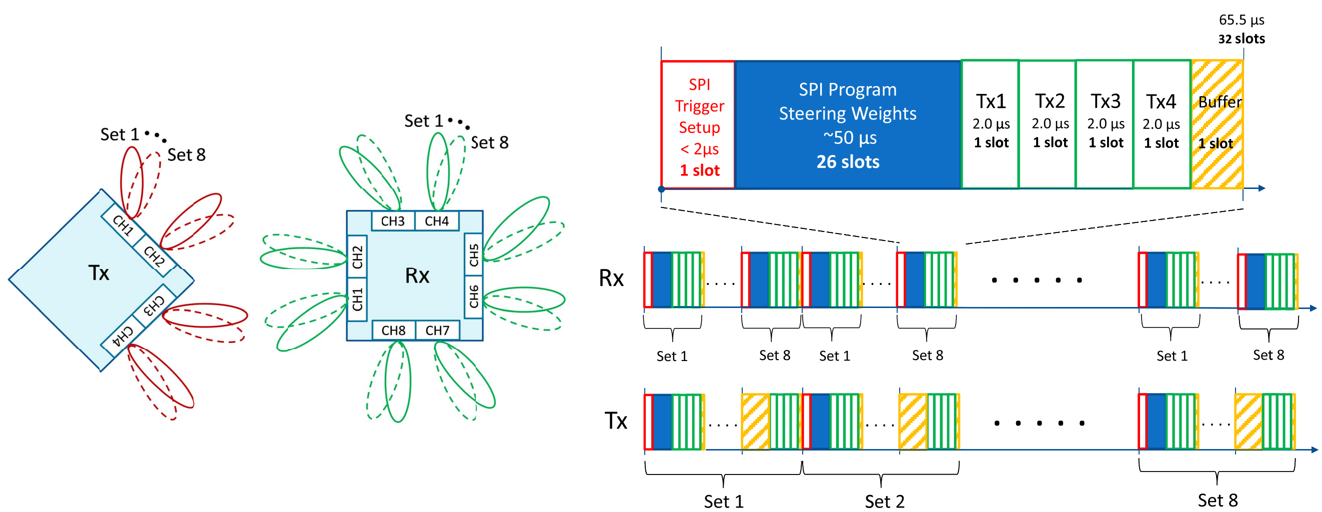

(a) (b)

Fig. 3. Channel sweep. For each set of Tx angles, a set of Rx angles is swept. There are eight unique Tx sets and eight unique Rx sets, hence a total of 64 unique Tx–Rx angle sets. (a) Tx angle sets and Rx angle sets. (b) Channel sweep schedule.

across the Tx channels so that the four angles in the same Tx set can be resolved; the eight Rx angles, on the other hand, are digitized simultaneously per Tx angle.

The Rx sets are cycled through while maintaining the Tx set constant; then, the Tx sets are cycled through. The resultant channel sweep requires 64 Tx–Rx sets $\times$ 32 slots $\times$ 2047 ns or $\Delta t = 4.19$ ms.

Thanks to direct digitization, the channel can be sampled at Δt, corresponding to a maximum measurable Doppler shift of $|\Delta f|_{\max} = (1/2\Delta t)$. Doppler shift is related to f_c and the maximum velocity between the transceivers that can be resolved as $|v|_{\max} = (|\Delta f|_{\max}/f_c) \cdot c$, where c is the speed of light. To deal with V2V scenarios, for which the Tx and Rx are mobile, the array size is reduced to 8×4 by deactivating

12 of the 16 columns (setting their magnitude to the lowest setting), effectively increasing the beamwidth to 22.5°. Hence, to span the ±45° range per board, 8 angles—4 angles per array covering +45° and −45° each—are swept instead. A complete channel sweep then only requires $\Delta t = 262$ μs so that a closing velocity up to $|v|_{\max} = 33$ km/h can be supported. This comes at the expense of 6 dB reduced gain per array, as well as reduction in angular precision due to the wider beamwidth.

E. Mobile Robot and Positioning System

The transmit section mounted on a tripod at 1.75 m and the receive section mounted on the mobile robot at 1.6 m are shown in Fig. 1(b). The autonomous robot, described in detail in [16], enables rapid data acquisition coupled with a navigational system—laser-guided indoors and military-grade GPS outdoors—that reports its position with centimeter accuracy, its velocity in units of 1 mm/s, and heading within 1°. The robot also generates a map of the environment to facilitate the development of map-based channel models [18] that can be verified through ray tracing.

III. System Calibration

To obtain the optimal channel-sounding performance, the nonideal effects of each system component—from the transmit and receive sections to the individual array boards—must be characterized and compensated. This is the topic of discussion for this section.

A. Characterization of Array Steering Weights

The array is steered electronically by modulating the phase shifters and amplifiers of its columns through the SPI controller, equivalent to applying complex weights. Each column weight is defined by a phase state (five bits) and a magnitude state (four bits) that are programmed independently. Although each state has a nominal value, the actual values may vary significantly between arrays due to different electrical path lengths and other sources of distortion [22]. As such, while the nominal phase value of the magnitude states is 0° and the nominal magnitude value of the phase states is unity, all states are actually complex valued, and a weight value is the multiplication of its phase value and its magnitude value. To optimize the beam patterns, the precise state values were characterized.

To that end, a vector network analyzer (VNA) and mmWave frequency extension modules were utilized. The measurements were conducted in an anechoic chamber (see Fig. 4) for which port 1 of the VNA was connected to a horn antenna and port 2 was connected to the array under inspection. The antennas were pointed toward each other at boresight at 3.323-m separation, well in their far field. Each column was activated individually (by setting its magnitude to the maximum nominal value while setting that of the other 15 columns to its minimum). Then, each phase state was cycled through, whose value was recorded as the S_{21} parameter at 62.5 GHz. Analogously, to measure the magnitude values of the column, its phase state was set to the nominal value of 0°

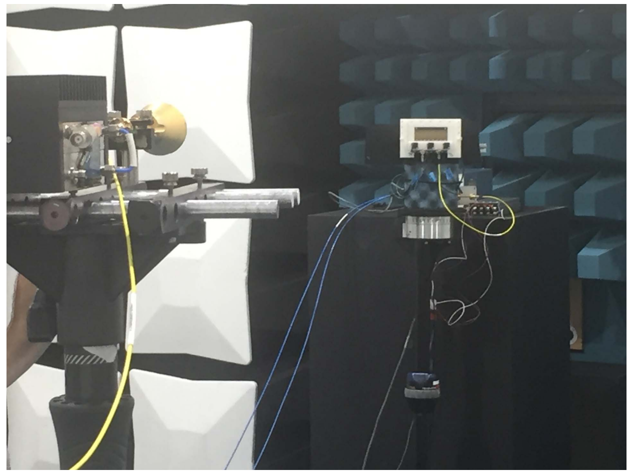

Fig. 4. OTA method for characterization of the array steering weights in an anechoic chamber. A horn antenna is used as a transmitter and the array under inspection as a receiver, driven by a VNA.

and the magnitude states were cycled through, for which the S_{21} parameters were recorded. This was repeated for every column. As the arrays operate in both transmit and receive modes—each mode has its own programmable phase shifters and amplifiers—a total of 1536 states were characterized per array.

With all state values in hand, the next step was to select the combination of phase and magnitude states across the columns that rendered the optimal beam pattern per steer angle θ_0. Phase was considered first: the objective was to minimize the sum of squared errors between the selected and ideal phase values across the 16 columns indexed through n

$$\sum_{n=1}^{16} \left(\phi_n^{\mathrm{sel}} - \phi_n^{\mathrm{ideal}}\right)^2 \tag{1}$$

where $\phi_n^{\mathrm{ideal}} = n\pi \cdot \sin\theta_0$. Once the optimal phase states were selected, the optimal magnitude states followed suite: the objective here was to achieve a uniform magnitude profile for the complex weights across the columns while accounting for the values of the phase states already selected.

A greedy optimization method was implemented to select the phase and magnitude states. With eight parallel processes, the state-characterization stage plus state-selection stage required 70 min of computation per steer angle per array. Although joint optimization of the phase and magnitude states in the selection stage may deliver better results, the associated time required was prohibitive.

B. Measurement of Array Beam Patterns

Once the array steering weights were computed, the resultant beam patterns were measured for all steer angles. The arrays on the transmit and receive sections were measured separately: similar to the previous setup, a horn antenna in the far field of the arrays was pointed toward an individual section; however, in this setup, the VNA was not used; rather, the PN code generated from the AWG was preferred to capture the wideband response of the arrays to the actual transmitted signal of the system. Another difference was that the sections

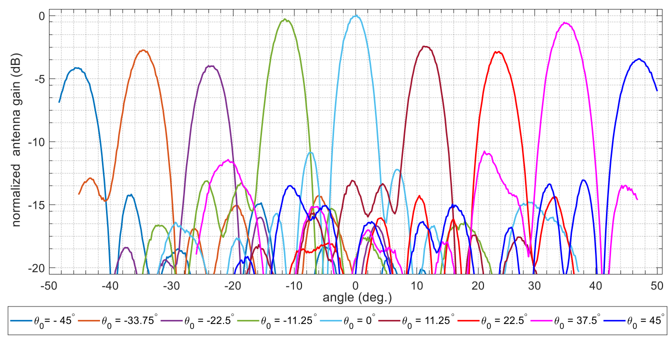

Fig. 5. Measured beam pattern at 11.25° increments for one of the phased-array antennas.

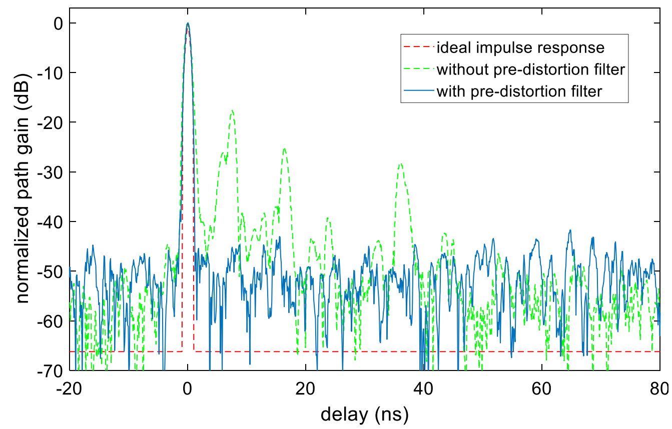

Fig. 6. Predistortion improves the dynamic range of the system by lowering the spurious peaks due to hardware nonidealities from −18 dB (green) to −45 dB (blue).

were placed individually on a turntable as a means to trace out the pattern sidelobes, as explained in the sequel.

Consider the receive section first. For each of its eight arrays, let $\hat{\theta}^{\text{Rx}}$ denote the angle of the array normal in the coordinate system of the robot. The arrays scanning negative angles were steered toward $\theta_i^{\text{Rx}} = \hat{\theta}^{\text{Rx}} - 45°\ldots\hat{\theta}^{\text{Rx}} - 5.6°$ in 5.6° increments, totaling eight steer angles indexed through i. This was repeated for the arrays scanning positive angles as $\theta_i^{\text{Rx}} = \hat{\theta}^{\text{Rx}}\ldots\hat{\theta}^{\text{Rx}} + 39.4°$. For each steer angle, the turntable was utilized to align the boresight of the steered pattern with the boresight of the horn (determined by where the detected power was strongest); the turntable was subsequently stepped out from $\theta^{\text{Rx}} = \theta_i^{\text{Rx}} - 180°\ldots\theta_i^{\text{Rx}} + 180°$ over the 360° FoV to record the steered beam pattern on a 0.25° grid (common to all Rx arrays). As we shall see later, this increment bounds the estimation precision for AoA. For each grid point θ^{Rx}, the PN code was transmitted from the horn and digitized at the array; the peak complex value from the output of the match filter was stored as $s_i^{\text{Rx}}(\theta^{\text{Rx}})$. The process was repeated for all arrays, yielding a total of 64 steer angles represented compactly through the receive steering vector $\boldsymbol{s}^{\text{Rx}}(\theta^{\text{Rx}}) = [s_1(\theta^{\text{Rx}})s_2(\theta^{\text{Rx}})\cdots s_{64}(\theta^{\text{Rx}})]$. Fig. 5 displays every other measured beam pattern—at 11.25° increments, not 5.6°, to avoid clutter such that the sidelobes can be seen clearly—for one of the arrays.

The process was analogous for the transmit section, resulting in the transmit steering vector $\boldsymbol{s}^{\text{Tx}}(\theta^{\text{Tx}}) = [s_1(\theta^{\text{Tx}})s_2(\theta^{\text{Tx}})\cdots s_{32}(\theta^{\text{Tx}})]$. Note that since there are just four transmit arrays, the dimension of the transmit steering vector is just 32 and $\theta^{\text{Tx}} = \theta_i^{\text{Tx}} - 90°\ldots\theta_i^{\text{Tx}} + 90°$ is stepped out on 0.25° grid (common to all Tx arrays) over the 180° FoV only.

C. Impulse Response Calibration

The transmit and receive sections have real hardware transfer functions that distort the ideal impulse response of the system, for which calibration is necessary. In our work, calibration is achieved through predistortion filtering, preferable to the alternative postdistortion filtering because it can be applied to high signal-to-noise conditions at the Tx to avoid boosting the noise level at the Rx.

The traditional means to design predistortion filters are through the back-to-back method: the transmit and receive sections are connected directly through a waveguide (or low-distortion cable) after removing the antennas. Next, the ideal PN code is transmitted, and the code distorted by the system is captured at the receiver. The distorted code is then deconvolved from the ideal code, yielding as a result the predistorted code. It follows that when the predistorted code is generated by the AWG and transmitted instead of the ideal code, the ideal code is received instead of the distorted code. The details of the design can be found in [17].

When dealing with phased-array antennas, the back-to-back method cannot be applied because the RF components in the SiGe chips on the printed circuit board—which also distort the system impulse response—are not accessible through connectors. As such, an OTA method was applied instead. The OTA method mimicked the operation of the sounder in the field: the wideband PN code was employed as well as the array antennas on both transmit and receive sections (the horn antenna was not used) to capture their nonidealities as well. Because there are four transmit array and eight receive arrays, a unique predistortion signal was computed for each of the 32 (4×8) pairs. For each pair, the arrays were steered at $\theta_0 = 0°$ and their boresights aligned. The predistorted signal was computed in the same manner as in the back-to-back method, except that the free-space loss (calculated from the Friis equation given the measured distance between the array phase centers) replaced the waveguide attenuation.

Fig. 6 shows the power-delay profile (path gain of the impulse response) of the ideal PN code normalized to 0 dB. Also shown are power-delay profiles with and without predistortion for an example Tx–Rx array pair: we can see that predistortion reduces the spurious peaks from −18 to −45 dB, extending the dynamic range by 27 dB. It was found that a single predistortion filter was acceptable per Tx–Rx array pair, valid across all steer angles.

D. Compensation for Clock Drift

Besides providing triggering for synchronous transmission and digitization across the Tx and Rx channels, the rubidium clocks also maintain phase stability to enable coherent combination across the Tx–Rx steer angles in a channel acquisition. Although extremely precise, the clocks will still suffer from timing drift. The timing drift between the clocks can be

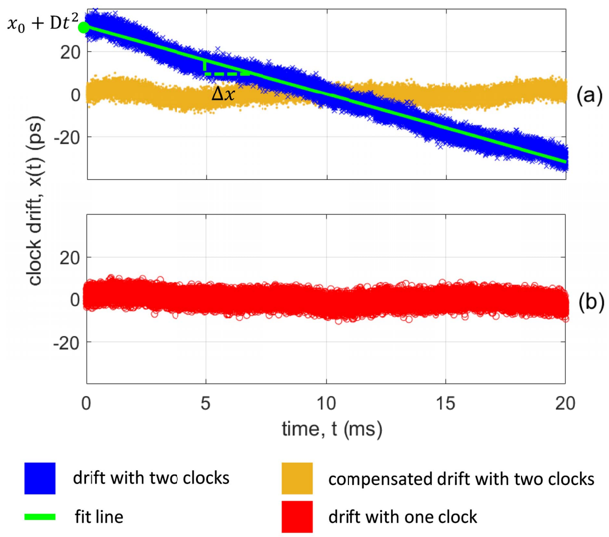

Fig. 7. Short-term timing stability of the measurement system. (a) Measured clock drift using two untethered rubidium clocks and drift compensated by fit line. (b) Measure drift using one rubidium clock.

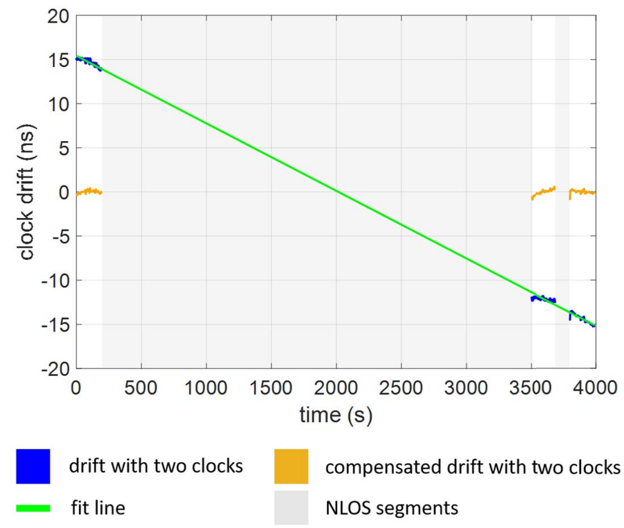

Fig. 8. Long-term timing stability during an outdoor measurement campaign. Measured clock drift in LOS and drift compensated by fit line. No data points are available in the NLOS segments, for which the clock drift must be extrapolated.

modeled as [26], [27]

$$x(t) = x_0 + \Delta x \cdot t + Dt^2 + N(t) \tag{2}$$

where x_0 is the initial time offset, Δx is the constant fractional frequency offset, D is the frequency drift rate ("aging") of the rubidium cell, and $N(t)$ is noise.

For the short-term time scale relevant to our channel sweep (on the order of milliseconds), D can be considered stationary and so aggregated with x_0, but Δx and $N(t)$ must be quantified. The latter was accomplished by transmitting a continuous-wave signal (narrowband to minimize the contribution of white noise) generated by the AWG and upconverted to 62.5 GHz, then downconverted back to IF and digitized while the clocks were free-running (untethered). We honed in on a peak of the received sinusoid and recorded its delay $x(t)$ over samples in time.

The blue plot shown in Fig. 7(a) shows the samples of $x(t)$ over a 20-ms interval. We can observe a constant slope, equivalent to the fractional frequency offset, whose value $\Delta x = -3.17$ ps/ms was found by fitting a line (in green) to the plot. Also highlighted in Fig. 7(a) is the extrapolated quantity $x_0 + Dt^2$. The fractional frequency offset was compensated by subtracting $x_0 + \Delta x \cdot t + Dt^2$ from (2), leaving the residual noise $N(t)$ shown in orange. The time Allan deviation (TDEV) [28] of the residual noise was computed as $\sigma_N = 0.25$ ps. Compare that to the red plot shown in Fig. 7(b) also showing samples of $x(t)$, however, with the Tx and Rx synchronized using a single clock (through tethering). While the red plot has no fractional frequency offset, it is still subject to noise, whose TDEV was computed as $\sigma_N = 0.38$ ps. This shows how the timing drift can be compensated and how operation in the untethered mode is then comparable to the tethered mode. At 62.5 GHz, the 0.25-ps TDEV of the untethered mode is equivalent to a standard deviation of 5.4° in phase noise.

The long-term clock drift (on the order of hours) is also important to gage because it is used in our system to estimate the absolute delay in nonline-of-sight (NLOS) conditions, as we shall see later (also see related work in [15]). In line-of-sight (LOS) conditions, the direct path can be detected and is easily recognized as the first and strongest path. Its measured delay is pinned to the ground-truth delay—equivalent to the Tx–Rx distance reported from the positioning system translated through the speed of light—to compensate for any drift. Since the positioning system is accurate to within centimeters, the ground-truth delay will be accurate to within fractions of a nanosecond. Besides for estimating absolute delay in LOS, this method also provides a means to compute the long-term clock drift as the measured delay subtracted from the ground-truth delay.

Fig. 8 shows the computed drift in blue during a measurement campaign outside in both LOS and NLOS conditions with the clocks free-running over more than one hour (4000 s).[1] A line (in green) with slope -0.0076 ps/ms was fit to the three LOS segments, where data points were available. The long-term slope is different from the short-term slope, Δx, previously reported for two main reasons: 1) the frequency drift rate, D, plays a role at this scale and 2) abrupt movement of the robot, in particular turning or traversing uneven ground, causes either positive or negative spikes from the short-term linear behavior shown in Fig. 7(a). Nevertheless, the standard deviation of the residual (in orange) between the fit line and data points was only 0.22 ns with a maximum value of 0.96 ns. Finally, the extrapolated clock drift was added to the measured delay as an estimate of the absolute delay in the two NLOS segments, where the direct path could not be detected due to high penetration loss at mmWave frequencies.

IV. MULIPATH-COMPONENT EXTRACTION

This section describes how the properties of the channel MPCs—delay, double-directional angle, and complex

[1]The data in the figure were actually generated from a measurement campaign with our 28-GHz switched-array channel sounder, but the clock performance is the same.

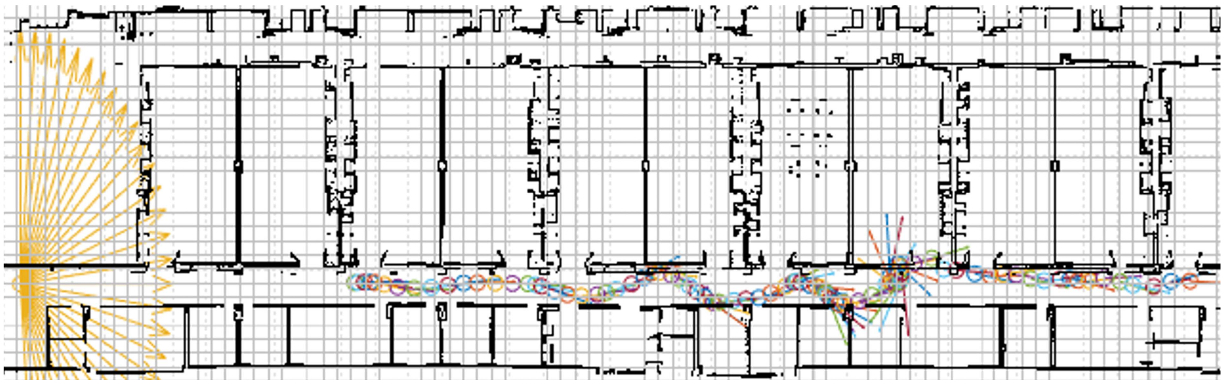

(a)

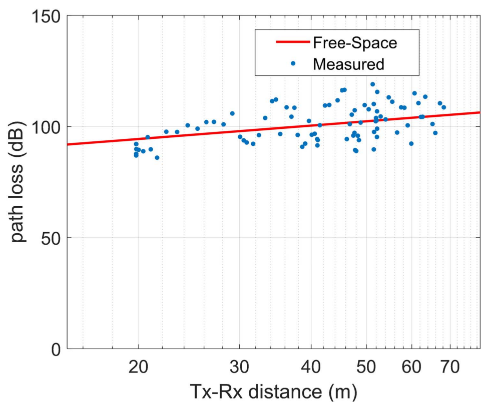

(b)

Fig. 9. Hallway measurements. (a) Display of zigzag Rx movement downs the hallway. The map (in black) was generated by the laser-guided navigation system of the robot. There were a total of 93 acquisitions, each shown as a circle with a different color. For each acquisition, the estimated robot heading is shown as an arrow in the coordinate system centered at the Tx (in orange at far left). (b) Path loss of the strongest peak detected at each acquisition versus distance.

amplitude—are extracted from field measurements. Using the same data structure as in Section II-B, a channel acquisition consists of 32×64 Tx–Rx steer angles. For each, the complex impulse response recorded as a function of delay, τ, is represented as an entry in the 32×64 matrix, $\boldsymbol{Y}(\tau)$. The projection of the received signal onto the transmit and receive vectors, $\boldsymbol{s}^T(\theta^T)$ and $\boldsymbol{s}^{\mathrm{Rx}}(\theta^{\mathrm{Rx}})$, respectively, is computed as

$$p(\tau, \theta^{\mathrm{Tx}}, \theta^{\mathrm{Rx}}) = \frac{\boldsymbol{s}^{\mathrm{Tx}}(\theta^{\mathrm{Tx}}) \cdot \boldsymbol{Y}(\tau)^* \cdot \boldsymbol{s}^{\mathrm{Rx}}(\theta^{\mathrm{Rx}})^t}{\|\boldsymbol{s}^{\mathrm{Tx}}(\theta^{\mathrm{Tx}})^t \cdot \boldsymbol{s}^{\mathrm{Rx}}(\theta^{\mathrm{Rx}})\|_F \cdot \|\boldsymbol{Y}(\tau)\|_F} \tag{3}$$

where $*$ denotes the complex conjugate and t the transpose operation.

For the sake of efficiency, the delay space was first searched to find peaks in $\|\boldsymbol{Y}(\tau)\|_F$; each peak was associated with a unique MPC. Then, for the kth delay peak, τ_k, the double-directional angle of the MPC was determined as

$$\left(\theta_k^{\mathrm{Tx}}, \theta_k^{\mathrm{Rx}}\right) = \underset{(\theta^{\mathrm{Tx}}, \theta^{\mathrm{Rx}})}{\arg\max}\, p\left(\tau_k \theta^{\mathrm{Tx}}, \theta^{\mathrm{Rx}}\right) \tag{4}$$

Finally, the complex amplitude of the MPC was calculated as

$$a_k = \frac{\boldsymbol{s}^{\mathrm{Tx}}\left(\theta_k^{\mathrm{Tx}}\right) \cdot \boldsymbol{Y}(\tau_k)^* \cdot \boldsymbol{s}^{\mathrm{Rx}}\left(\theta_k^{\mathrm{Rx}}\right)^t}{\left\|\boldsymbol{s}^{\mathrm{Tx}}\left(\theta_k^{\mathrm{Tx}}\right)^t \cdot \boldsymbol{s}^{\mathrm{Rx}}\left(\theta_k^{\mathrm{Rx}}\right)\right\|_F}. \tag{5}$$

Note that (5) de-embeds the transmit and receive array beam patterns such that, together with predistortion filtering, a_k represents the pure response of the channel alone not including the system.

A. Test Results

Two sets of measurements were collected in LOS conditions to showcase the functionality of the system. The first set was in a hallway: 93 acquisitions were recorded up 70 m (the length of the hallway). The map generated by the robot is shown in Fig. 9(a). The robot moved in a zigzag pattern to vary the AoD/AoA of the paths (relative to the robot heading). For each acquisition, the strongest peak was detected and its path loss plotted versus the Tx–Rx distance shown in Fig. 9(b). While the plot follows the free-space curve well, the standard deviation due to fading is 4.7 dB. The fading was caused by the direct path combining with the ground, ceiling, and wall reflections, all arriving within the 1-ns delay resolution of the system at these distances.

For each acquisition, distinct channel MPCs were detected strongly by at least nine (3×3) Tx–Rx steer angle pairs. Fig. 10(a) shows an acquisition at 21 m for illustrative purposes: the Tx_{17}–Rx_9 steer angle is the best aligned with the AoD/AoA of the direct path since the first path detected in the nine power-delay profiles is strongest in $Y_{17,9}(\tau)$. Accordingly, the strength of the direct path for the other eight Tx–Rx steer angles is proportional to their alignment with the direct path. By comparing their relative strength—as quantified by $p(\tau, \theta^{\mathrm{Tx}}, \theta^{\mathrm{Rx}})$—the double-directional angle can be estimated beyond the half-power beamwidth of the arrays. Note that other MPCs besides the direct path are also detected

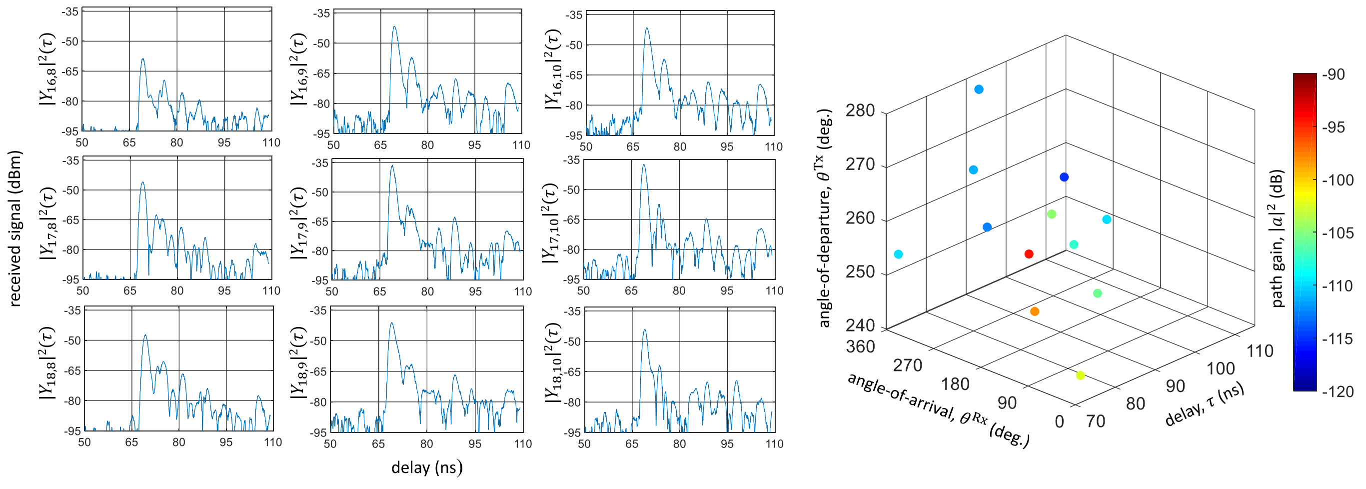

(a) (b)

Fig. 10. Illustrative acquisition at a Tx–Rx distance of 21 m in the hallway. (a) Recorded power-delay profiles for nine (3 × 3) Tx–Rx steer angles. (b) MPCs extracted by combining all profiles in the acquisition.

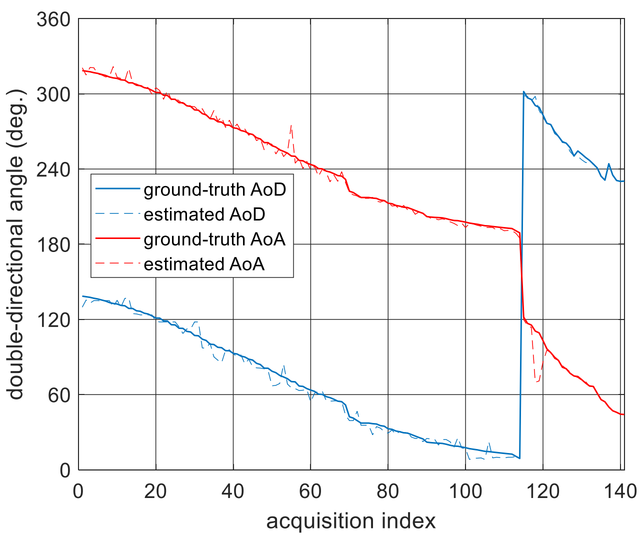

Fig. 11. Double-directional angle estimation. The robot was rotated to exhaustively test its FoV and estimation capability for the AoD/AoA of the direct path against the ground-truth values reported from the robot's navigation system.

in the responses. The properties of all MPCs extracted are displayed in the power-angle-delay profile shown in Fig. 10(b).

The second set of measurements was collected in our lab—a more open space than the hallway where the robot had sufficient leeway to turn—at distances less than 10 m so that the direct path could be easily resolved from the ambient reflections. The purpose was to exhaustively vary the double-directional angle of the direct path, whose ground-truth values are given from the Tx orientation and the robot's heading. Fig. 11 shows the jointly estimated AoD/AoA versus their ground-truth values over 141 acquisitions. The values track each other well, with a mean error of 3.15°/2.58° for AoD/AoA. Keep in mind that a component of the error—up to 1°—stems from the ground-truth error in the heading reported from the positioning system, so the estimated angle error is actually lower. Finally, notice the omnidirectional FoV of the Rx and the 180° FoV of the Tx over the acquisitions.

V. Conclusion

The essential requirements for 5G channel sounding are high directional antenna gain, omni-double-directional scanning capabilities, high angular resolution, ultrawide bandwidth, and fast channel sweep period. In this paper, we presented a 60-GHz phased-array-antenna system that meets those requirements, the first of its kind. To deliver such angular resolution, we proposed OTA methods to calibrate the antennas and measure their patterns, as well as apply predistortion filtering to maximize the dynamic range of the system. The system yielded a mean absolute angle error of 2.87° in exhaustive test measurements. For V2V scenarios, the system can be operated to record full channel sweep in just 262 μs, supporting a maximum closing velocity of 33 km/h.

So far, predistortion filtering has only been applied to the boresight steer angles of each Tx–Rx array. To optimize the performance yet further, we plan to apply filtering over all steer angles of each Tx–Rx array.

References

[1] Federal Commun. Commission (FCC), Washington, DC, USA, Tech. Rep. FCC-16-89, Jul. 2016.

[2] Standard IEEE 802.11ay Amendment. [Online]. Available: http://www.ieee802.org/11/Reports/tgay_update.htm

[3] S. Deng, G. R. MacCartney, and T. S. Rappaport, "Indoor and outdoor 5G diffraction measurements and models at 10, 20, and 26 GHz," in *Proc. IEEE Global Commun. Conf.*, Dec. 2016, pp. 1–7. doi: 10.1109/GLOCOM.2016.7841898.

[4] A. Bodi, J. Zhang, J. Wang, and C. Gentile, "Physical-layer analysis of IEEE 802.11ay based on a fading channel from mobile measurements," in *Proc. IEEE Int. Conf. Commun.*, May 2019, pp. 1–7.

[5] C. Gentile, P. B. Papazian, R. Sun, J. Senic, and J. Wang, "Quasi-deterministic channel model parameters for a data center at 60 GHz," *IEEE Antennas Wireless Propag. Lett.*, vol. 17, no. 5, pp. 808–812, May 2018.

[6] S. A. Saberali and N. C. Beaulieu, "New expressions for TWDP fading statistics," *IEEE Wireless Commun. Lett.*, vol. 2, no. 6, pp. 643–646, Dec. 2013.

[7] A. Maltsev, R. Maslennikov, A. Sevastyanov, A. Khoryaev, and A. Lomayev, "Experimental investigations of 60 GHz WLAN systems in office environment," *IEEE J. Sel. Areas Commun.*, vol. 27, no. 8, pp. 1488–1499, Oct. 2009.

[8] H. Sawada, H. Nakase, S. Kato, M. Umehira, K. Sato, and H. Harada, "Impulse response model and parameters for indoor channel modeling at 60 GHz," in *Proc. IEEE 71st Veh. Technol. Conf.*, May 2010, pp. 1–5.

[9] S. Hur, Y.-J. Cho, J. Lee, N.-G. Kang, J. Park, and H. Benn, "Synchronous channel sounder using horn antenna and indoor measurements on 28 GHz," in *Proc. IEEE Int. Black Sea Conf. Commun. Netw.*, May 2014, pp. 83–87.

[10] M. R. Akdeniz *et al.*, "Millimeter wave channel modeling and cellular capacity evaluation," *IEEE J. Sel. Areas Commun.*, vol. 32, no. 6, pp. 1164–1179, Jun. 2014.

[11] J. J. Park *et al.*, "Millimeter-wave channel model parameters for urban microcellular environment based on 28 and 38 GHz measurements," in *Proc. IEEE 27th Annu. Int. Symp. Pers., Indoor, Mobile Radio Commun. (PIMRC)*, Sep. 2016, pp. 1–5.

[12] B. N. Liya and D. G. Michelson, "Characterization of multipath persistence in device-to-device scenarios at 30 GHz," in *Proc. IEEE Global Commun. Conf.*, Dec. 2016, pp. 1–6.

[13] D. Dupleich *et al.*, "Directional characterization of the 60 GHz indoor-office channel," in *Proc. 31st URSI General Assembly Sci. Symp.*, Aug. 2014, pp. 1–4.

[14] D. Dupleich, J. Luo, S. Haefner, R. Mueller, C. Schneider, and R. Thomae, "A hybrid polarimetric wide-band beam-former architecture for 5G mm-wave communications," in *Proc. 20th Int. ITG Workshop Smart Antennas*, Mar. 2016, pp. 1–8.

[15] G. R. MacCartney and T. S. Rappaport, "A flexible millimeter-wave channel sounder with absolute timing," *IEEE J. Sel. Areas Commun.*, vol. 35, no. 6, pp. 1402–1418, Jun. 2017.

[16] A. W. Mbugua, W. Fan, Y. Ji, and G. F. Pedersen, "Millimeter wave multi-user performance evaluation based on measured channels with virtual antenna array channel sounder," *IEEE Access*, vol. 6, pp. 12318–12326, 2018.

[17] R. Sun *et al.*, "Design and calibration of a double-directional 60 GHz channel sounder for multipath component tracking," in *Proc. 11th Eur. Conf. Antennas Propag.*, Mar. 2017, pp. 3336–3340.

[18] A. Maltsev *et al.*, "Quasi-deterministic approach to mmWave channel modeling in a non-stationary environment," in *Proc. IEEE Globecom Workshops*, Dec. 2014, pp. 966–971.

[19] P. B. Papazian, C. Gentile, K. A. Remley, J. Senic, and N. Golmie, "A radio channel sounder for mobile millimeter-wave communications: System implementation and measurement assessment," *IEEE Trans. Microw. Theory Techn.*, vol. 64, no. 9, pp. 2924–2932, Sep. 2016.

[20] Z. Wen *et al.*, "mmWave channel sounder based on COTS instruments for 5G and indoor channel measurement," in *Proc. IEEE Wireless Commun. Netw. Conf.*, Apr. 2016, pp. 1–7.

[21] S. Salous, S. M. Feeney, X. Raimundo, and A. A. Cheema, "Wideband MIMO channel sounder for radio measurements in the 60 GHz band," *IEEE Trans. Wireless Commun.*, vol. 15, no. 4, pp. 2825–2832, Apr. 2016.

[22] B. Rupakula, A. Nafe, S. Zihir, Y. Wang, T.-W. Lin, and G. Rebeiz, "63.5–65.5-GHz transmit/receive phased-array communication link with 0.5–2 Gb/s at 100–800 m and $\pm$ 50° scan angles," *IEEE Trans. Microw. Theory Techn.*, vol. 66, no. 9, pp. 4108–4120, Sep. 2018.

[23] R. J. Weiler *et al.*, "Millimeter-wave outdoor access shadowing mitigation using beamforming arrays," in *Proc. 10th Eur. Conf. Antennas Propag. (EuCAP)*, Apr. 2016, pp. 1–5.

[24] C. U. Bas *et al.*, "Dynamic double directional propagation channel measurements at 28 GHz," in *Proc. IEEE 87th Veh. Technol. Conf.*, Jun. 2018, pp. 1–6.

[25] C. Slezak, V. Semkin, S. Andreev, Y. Koucheryavy, and S. Rangan, "Empirical effects of dynamic human-body blockage in 60 GHz communications," *IEEE Commun. Mag.*, vol. 56, no. 12, pp. 60–66, Dec. 2018.

[26] W. J. Riley, "Handbook of frequency stability analysis," NIST, Gaithersburg, MD, USA, Tech. Rep. NIST SP-1065, Jul. 2008, p. 19.

[27] D. W. Allan, D. D. Davis, J. Levine, M. A. Weiss, N. Hironaka, and D. Okayama, "New inexpensive frequency calibration service from NIST," in *Proc. 44th Annual Symp. Freq. Control*, May 1990, pp. 107–116.

[28] D. W. Allan, M. A. Weiss, and J. L. Jespersen, "A frequency-domain view of time-domain characterization of clocks and time and frequency distribution systems," in *Proc. 45th Annu. Symp. Freq. Control*, May 1991, pp. 667–678.

Derek Caudill received the B.S. degree in electrical engineering and the M.S. degree in electrical and computer engineering from the University of Massachusetts Amherst, Amherst, MA, USA, in 2016 and 2017, respectively.

He was a Research Associate with the Communications Technology Laboratory, NIST, where he supports the data acquisition efforts of millimeter-wave (mmWave) channel model measurements and the systems that such measurements depend on.

Peter B. Papazian (SM'98) received the B.S. degree in physics from the State University of New York Stonybrook, Stony Brook, NY, USA, in 1973, and the M.S. degree from the Colorado School of Mines, Golden, CO, USA, in 1979.

He is currently the 5G Millimeter-Wave (mmWave) Channel Sounder Project Leader with the NIST Communications Technology Laboratory, Boulder, CO, USA. The purpose of his research is to conduct mmWave radio channel propagation measurements to support model and standard development for 5G radio systems.

Camillo Gentile (M'01) received the B.S. and M.S. degrees in electrical engineering jointly from Drexel University, Philadelphia, PA, USA, in 1996, and the Ph.D. degree in electrical engineering from Pennsylvania State University, University Park, PA, USA, in 2001.

In 2001, he joined the National Institute of Standards and Technology, Gaithersburg, MD, USA, where he is currently a Project Leader with the Wireless Networks Division, Communications Technology Laboratory. He has authored over 70 peer-reviewed journals and conference papers and 1 book on geolocation techniques. His current interests include channel modeling and physical-layer modeling for 5G communication systems.

Jack Chuang received the Ph.D. degree in electrical engineering from Pennsylvania State University, University Park, PA, USA, in 2008.

He was a Graduate Research Assistant with the Communications and Space Sciences Laboratory (CSSL), Pennsylvania State University. He was then with BAE Systems, where he was involved in electronic warfare, and with Cisco Systems, where he was involved in spectrum sharing. He is currently with the NIST Communications Technology Laboratory, Gaithersburg, MD, USA, developing 5G millimeter-wave (mmWave) channel sounders.

Nada Golmie received the Ph.D. degree in computer science from the University of Maryland at College Park, College Park, MD, USA.

She serves as a Co-Chair for the 5G Millimeter-Wave (mmWave) Channel Model Alliance. She is currently the Chief of the Wireless Networks Division, Communications Technology Laboratory, National Institute of Standards and Technology, Gaithersburg, MD, USA. Her current research interests include media access control and protocols for wireless networks has led to over 100 technical papers presented at professional conferences and journals.